CellPress

Trends in Chemistry

Review

The halogen chemistry of halide perovskites

Roc Matheu [1,4], Julian A. Vigil [1,2,4], Ethan J. Crace,[1] and Hemamala I. Karunadasa [1,3,*]

The oxygen chemistry of oxide perovskites has been studied for decades, revealing reactivity, transport, and electronic properties enabled by the oxide anion. Similarly, the halide anion dictates the properties and unusual phenomena observed in halide perovskites. Manipulating the halide site has improved the performance and stability of halide perovskites in a range of optoelectronic technologies, most commonly as components in solar cells and light-emitting diodes. Further, the redox activity of the halides allows for controlled electronic doping and halide exchange, as well as for the capture and separation of halogen gases. Herein, we summarize the key aspects of the chemistry of the perovskite halide site. We close with a discussion of pseudohalide perovskites, which hold commonalities with the halide perovskites.

Highlights

In analogy to the role of the oxide anion in oxide perovskites, the halogen chemistry of halide perovskites significantly contributes to the chemical, physical, and optoelectronic properties of this class of materials.

Investigating and manipulating the halide site has improved our understanding of the electronic structure, reactivity, defect chemistry, and ionic conductivity of halide perovskites.

A clear understanding of the chemistry of the halide site is expected to (i) yield novel perovskites with targeted optoelectronic properties and controlled defect chemistry, (ii) improve the efficiency and stability of perovskite optoelectronic devices, and (iii) expand the scope of postsynthetic reactions between perovskites and small molecules.

Halide perovskites

Perovskites are crystalline solids with the general formula ABX_3, where X is an anionic ligand such as oxide, chalcogenide, or halide. Historically, oxide perovskites have received the most attention in this family of materials. Although halide perovskites are also not new—dating back to the 1800s [1–4]—their study has recently been invigorated through the discovery of their outstanding semiconducting properties. The lead-halide perovskites have emerged as candidates for high-efficiency and low-cost solar absorbers [5–7], while other applications such as phosphors [8,9], light-emitting diodes [10,11], and scintillators [12] have also shown promise.

The halide site dictates many of the defining characteristics of halide perovskites: solution-state self-assembly, stabilization of low-valent metals, soft lattices with **bulk moduli** (see Glossary) that can be as small as those of organic molecules, structures that exhibit fast and slow dynamics, and electronic structures that commonly yield shallow trap states. Indeed, manipulating the halide site has enabled key optoelectronic properties to be optimized [e.g., optical bandgap and photoluminescence (PL) color, electronic transport, and defect chemistry], has explained unusual phenomena observed in perovskite-based devices (e.g., halide conductivity and light-induced halide segregation in mixed-halide compositions), and has resulted in new materials and applications (e.g., radioactive I_2 capture, halogen gas separation). Here, we compile our understanding of the halogen chemistry of halide perovskites. We describe the role of the halogen in dictating perovskite structure, optical absorption and emission, electronic and ionic transport, defect chemistry, and reactivity with small molecules. We conclude by briefly reviewing the closely related pseudohalide perovskites. We refer interested readers to recent reviews on halide conductivity [13], photo-induced **phase segregation** [14,15], pseudohalide perovskites [16], and halogen gas capture and separation in perovskites [17].

The oxygen chemistry of oxide perovskites

Halide perovskites are structural analogs of oxide perovskites, such as $CaTiO_3$. Substitutions at the A- and B-sites of ABO_3 oxide perovskites have led to important applications in electroceramics, including dielectrics and piezoelectrics [18]. Non-stoichiometry at the oxide site (e.g., $ABO_{3\pm\delta}$) and oxygen point defect reactions, however, are appreciated for their role in modern discoveries, including high-temperature cuprate superconductors [19]. A detailed

[1]Department of Chemistry, Stanford University, Stanford, CA 94305, USA
[2]Department of Chemical Engineering, Stanford University, Stanford, CA 94305, USA
[3]Stanford Institute for Materials and Energy Sciences, SLAC National Laboratory, Menlo Park, CA 94025, USA
[4]These authors contributed equally

*Correspondence: hemamala@stanford.edu (H.I. Karunadasa).

treatment of the chemistry of the oxide site has afforded a good understanding of the bonding and electronic structure, electronic and ionic transport, and reactivity of oxide perovskites. As members of the same materials family, parallels in the role of the X-site can be made between the oxide and halide perovskites.

The critical temperature (T_c) for superconductivity in $YBa_2Cu_3O_{7-\delta}$ is sensitive to the local Cu–O coordination changes induced by oxygen non-stoichiometry [20]; further, interactions between electronic charge carriers and oxygen defects influence the T_c upon aliovalent doping of La_2CuO_4 (i.e., $La_{2-x}M_xCuO_4$, M = Ba^{2+}, Sr^{2+}) [21,22]. The proposed mechanism for superconductivity in these two perovskites involves holes forming O^- ($O^{2-} + h^+$) or O_2^{2-} peroxo dimers [21]. Conversely, at elevated temperatures, oxygen-vacancy–mediated transport enables oxide conductivity in solid electrolytes such as alloyed and doped $LaMO_3$ (M = Ga^{3+}, Al^{3+}, In^{3+}, Sc^{3+}, Y^{3+}) perovskites [23]. The electronic and ionic transport properties of halide perovskites are similarly sensitive to halogen point defects and halide site occupancy.

Oxygen exchange is a critically important defect reaction that describes the equilibrium between the oxide lattice, oxygen vacancies, electrons, and gaseous O_2

$$2O_O^X \rightleftharpoons 2V_O^{\bullet\bullet} + 4e' + O_{2(g)} \quad [1]$$

where O_O^X is the pristine oxygen lattice site, $V_O^{\bullet\bullet}$ is a dicationic oxygen vacancy, and e′ is an electron (given in the Kröger–Vink notation). Manipulating this equilibrium through the O_2 partial pressure and temperature (generally >700 K) has improved our understanding of oxide diffusion and the thermodynamics of ionic and electronic conductivity [22]. The rational design of complex oxide perovskites, for instance to promote or resist oxygen exchange, has been informed by composition-dependent diffusion kinetics and thermodynamic modeling of dopants. Halide perovskites exhibit analogous point defect reactions, with particularly low activation barriers for the formation of halogen vacancies, calling for similar chemical approaches to improve stability. Thus, uncovering the parallels between the chemistry of oxide perovskites and that of their halide congeners should promote a deeper understanding of the latter (see Outstanding questions).

Halide contribution to the perovskite structure

Halide perovskites that adopt the 3D ABX_3 structure feature B-sites with octahedral coordination to six halides (X); each halide bridges two B-sites to afford an anionic BX_3^- framework of corner-sharing octahedra. Organic and/or inorganic A-site monocations reside in the cuboctahedral voids, providing charge compensation (Figure 1A). The B site is occupied by a 2+ metal in the ABX_3 single perovskites (e.g., Pb^{2+}, Hg^{2+}, Mn^{2+} [9]), whereas two distinct B and B′ sites alternate in the $A_2BB'X_6$ double perovskites, affording an average charge of 2+ (e.g., Ag^+ and Bi^{3+} or Sn^{4+} and a vacancy; Figure 1B) [24]. The 2D perovskites are related to the 3D structure through the formal addition of an AX salt (ABX_3 + AX ➔ A_2BX_4), resulting in both bridging and terminal halides as the inorganic sheets are separated by larger A-site cations (Figure 1C) [25,26].

Linus Pauling's radius ratio rules dictate the size of the cation that can support octahedral coordination of a given halide. Thus, as the anion/cation radius ratio increases, lower coordination numbers are preferred. For example, we are not aware of iodide perovskites with B-site cations as small as Mn^{2+} or Cd^{2+}. However, $CsCdX_3$ (X = Cl^-, Br^-) and $KMnCl_3$ crystallize as perovskites with the smaller halides [27–29]. Similarly, the Goldschmidt tolerance factor [30], also derived from geometric considerations, identifies limits to A-site–cation radius based on the B-site–cation and halide radii [31,32]. Compositions that deviate from the tolerance factor for an ideal, undistorted perovskite, with 180° B–X–B angles (Figure 1B), will either adopt a

Glossary

Bulk modulus (K_0): the bulk modulus at ambient pressure, a measure of a material's susceptibility to compression.
Color rendering index (CRI): a measure of a light source's ability to accurately reproduce illuminated colors.
Correlated color temperature (CCT): the temperature at which an ideal blackbody emits light of the same color as the emission.
Frenkel disorder (defect reaction): the displacement of an ion from an occupied lattice site to an unoccupied interstitial site; anti-Frenkel disorder refers to this defect reaction occurring in the anionic sublattice.
Ionic point defect: localized intrinsic (vacancies, interstitials, antisite defects) or extrinsic (e.g., substitutional impurities) defects in an ionic crystal, often characterized as zero dimensional and non-interacting.
Phase segregation: the separation of a single thermodynamic (or kinetically trapped) crystallographic phase into multiple distinct phases.
Schottky disorder (defect reaction): the formation of two oppositely charged vacancy defects.

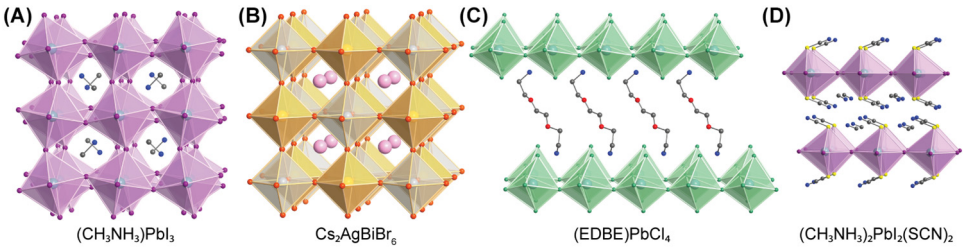

Figure 1. Crystal structures of halide perovskites exhibiting a range of dimensionality, symmetry, and composition. (A) A 3D halide perovskite in a tetragonal space group, $(CH_3NH_3)PbI_3$. (B) A 3D halide double perovskite in a cubic space group, $Cs_2AgBiBr_6$. (C) A 2D halide perovskite, (EDBE)$PbCl_4$. (D) A 2D halide-pseudohalide perovskite, $(CH_3NH_3)_2PbI_2(SCN)_2$. Octahedra comprising PbI_6 [including $PbI_4(SCN)_2$], $PbCl_6$, $AgBr_6$, and $BiBr_6$ are shaded in purple, green, white, and orange, respectively. Disordered atoms and hydrogen atoms are omitted for clarity. Key: pink, Cs; blue, N; red, O; gray, C; yellow, S. Abbreviation: EDBE, 2,2′-(ethylenedioxy)bis(ethylammonium).

lower-symmetry perovskite structure (e.g., with tilted octahedra) (Figure 1A) or a non-perovskite structure [33].

In analogy to the effects of hydrostatic pressure or temperature, the halide composition can also direct preferential crystallization of desired crystallographic phases. For example, Cs-substitution has been shown to induce a cubic-to-tetragonal phase transition in $[CH(NH_2)_2]_yCs_{1-y}Pb(Br_xI_{1-x})_3$ perovskite thin films [34]. Further increasing the effective radius of the A-site cation separates the metal–halide octahedra. This is often achieved with organoammonium cations and their effective size, charge, and shape determines the dimensionality (0D, 1D, 2D) and connectivity (corner-, edge-, face-sharing) of the metal–halide octahedra [26]. Halogen bonding can also template the crystallization of 2D perovskites. For example, interactions between organohalogens and inorganic halides direct the assembly of some 2D perovskites [35,36]. Lighter halides are reported to preferentially occupy the bridging sites in mixed-halide 2D perovskites, whereas heavier halides tend to occupy the terminal sites [37,38].

Halide contribution to the perovskite electronic structure

The electronic structure of halide perovskites is mainly set by the B-site metal and the halide. In lead-halide perovskites, lead s-orbitals and halide p-orbitals compose the valence band, whereas the conduction band primarily comprises lead p-orbitals (Figure 2A) [39,40]. The presence of lead, iodine, and other high-atomic-number elements in the perovskite structure necessitates treatment of spin–orbit coupling effects for accurate band structures and has motivated the study of various relativistic phenomena, including Rashba–Dresselhaus spin-splitting at the band edges [41]. Alloying at the halide site in 3D perovskites produces solid solutions of Cl^-/Br^- perovskites and Br^-/I^- perovskites, evidenced by powder X-ray diffraction measurements showing a continuous lattice expansion as larger halides are alloyed. Further, the absorption spectra of mixed-halide perovskites show a continuous shift in absorption onset with halide ratio for most compositions, although a discontinuity has been observed for $x = 0.5$ in $(CH_3NH_3)Pb(Br_xI_{1-x})_3$ films, attributed to imperfect mixing (Figure 2B) [42]. Because of the larger halide contribution to the valence band, the bandgap can be increased by substituting more electronegative halides (Figure 2A). For example, the bandgaps of 3D lead-halide perovskites can vary between 1.5 (for iodides) and 3.0 eV (for chlorides), while mixed-halide compositions show intermediate gaps (Figure 2B) [26].

The importance of halide–halide interactions is evident in double perovskites with vacant B sites (□), such as $A_2Sn□X_6$. Although these materials are structurally 0D, they display small bandgaps and large band dispersion. Their 3D electronic structure arises from 90° interactions between

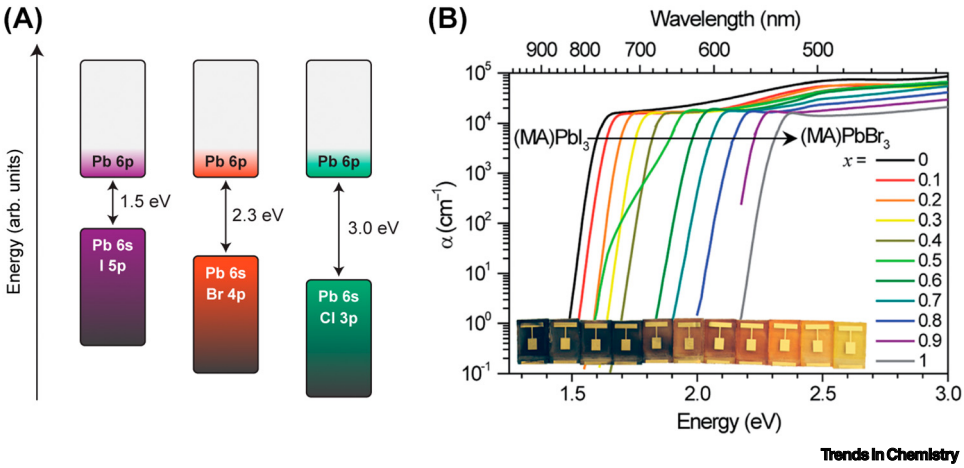

Figure 2. Influence of the halide site in the optoelectronic properties of halide perovskites. (A) Schematic block band diagram for 3D Pb–X perovskites (X = Cl^-, Br^-, I^-) highlighting the halide orbital contribution to the bandgap and the band extrema. (B) Absorption coefficient (α) for $(CH_3NH_3)Pb(Br_xI_{1-x})_3$ measured by diffuse reflectance and transmission measurements of thin films and photocurrent spectroscopy of solar cells (MA = $CH_3NH_3^+$). Inset: photographs of $(CH_3NH_3)Pb(Br_xI_{1-x})_3$ photovoltaic devices from $x = 0$ to $x = 1$ (left to right). (B) Reproduced, with permission, from [42].

halides across vacant B sites [43]. For 3D perovskites, monovalent cations that fit the A-site cavity [e.g., $CH_3NH_3^+$, Cs^+, $CH(NH_2)_2^+$] are few and only contribute to the electronic structure by inducing structural distortions in the inorganic framework. Varying the A-site composition can either increase the optical bandgap by tilting the BX_6^{n-} octahedra, or decrease the bandgap upon lattice contraction [44].

The 2D perovskites exhibit similar orbital contributions to the band edges as their 3D counterparts [39], but due to electronic confinement effects, photoexcitation produces excitons (bound electron–hole pairs) instead of free charge carriers. Excitons manifest as sharp peaks below the bandgap absorption onset. With halide alloying, the excitonic absorption peak also shows a continuous blueshift from ~2.3 eV for the pure Pb–I to ~3.6 eV for the pure Pb–Cl 2D perovskites and the excitonic PL tracks similarly [45]. The width of the excitonic absorption peak has been used as an indicator of local halide variation in $(PEA)_2PbCl_xBr_{4-x}$ and $(PEA)_2PbBr_xI_{4-x}$ (PEA = phenethylammonium) [45,46]. Here, the pure halides show narrow peaks, and the broader peaks seen in mixed-halide compositions have been attributed to locally disordered halides that change the potential energy landscape sampled by the exciton. Most 2D lead-halide perovskites show intense, narrow excitonic PL with high color purity, promising for phosphor applications, with the halides modulating the emission color [45]. For example, in $(PEA)_2PbX_4$, X = I^- produces green light, whereas X = Br^- yields blue light. Certain 2D perovskites also emit broadband white light [47]. Here too, halide mixing can tune the **color rendering index (CRI)** and **correlated color temperature (CCT)** of the emission. For example, in the prototypical white-light–emitting perovskite (*N*-MEDA)$PbCl_xBr_{4-x}$ (*N*-MEDA = N^1-methylethane-1,2-diammonium), the CRI was improved from 82 (x = 0) to 85 (x = 0.5) with halide mixing in isostructural analogs [48]. Likewise, the chloride and bromide derivatives of (EDBE)PbX_4 (Figure 1C) afford "cold" (CCT = 5509 K) and "warm" (CCT = 3990 K) white light, respectively, although here the chloride perovskite adopts the flat (001) perovskite sheets and the bromide perovskite adopts the corrugated (110) perovskite sheets [49].

Halide conductivity

Many of the phenomena highlighted in this review require significant halide conductivity, particularly for bulk reactions in 3D perovskites where, unlike in many 2D perovskites, there is no organic

layer to facilitate ion transport or volume expansion. Indeed, halide conductivity is invoked to explain anomalous behavior observed in 3D perovskite-based devices including current–voltage hysteresis [50,51], switchable photovoltaic effects [52], large low-frequency dielectric responses [44,53,54], and band bending and alignment at interfaces [55,56].

Ionic semiconductors exhibit varying degrees of ionic conductivity owing to structural disorder and the mobility of ions and **point defects** (see Figure IA,B in Box 1). The mixed ionic-electronic conductivity of inorganic halide perovskites was established in the 1980s [57]. The initial work was motivated by oxide perovskite and antiperovskite analogs exhibiting oxide conductivity, with structural data suggesting large displacements of the oxide anion. Mizusaki and colleagues [57] reported significant halide conductivity for $CsPbX_3$ (X = Cl^-, Br^-) and $KMnCl_3$ and proposed halogen vacancies as the mobile species based on gravimetric changes of coulometric reaction cells (see Figure IC,D in Box 1). The activation energy (E_a) of halogen vacancy migration was relatively small for $CsPbX_3$ (X = Cl^-, Br^-; 0.25-0.29 eV) and for $KMnCl_3$ (0.39 eV) [57]. Halide conductivity was later suggested in the hybrid perovskites: $(CH_3NH_3)MCl_3$ (M = Ge^{2+}, Sn^{2+}) [58,59] and $(CH_3NH_3)PbX_3$ (X = Cl^-, Br^-) [60]. Halide conductivity in $(CH_3NH_3)PbI_3$ had been extensively discussed [50,52,61]; however, bulk ionic conductivity measurements were not directly revisited until 2015 by Maier, Gregori, and colleagues [44]. Polycrystalline $(CH_3NH_3)PbI_3$ exhibits significant ionic conductivity in the dark and the iodine vacancy was established as the dominant mobile defect from a reaction cell (see Figure ID in Box 1) [12,44]. Iodine vacancies were confirmed as the dominant mobile defect in $(CH_3NH_3)PbI_3$ based on the dependencies of the ionic conductivity on I_2 partial pressure [$p(I_2)$] and acceptor doping, as well as various solid-state NMR measurements [12,62,63].

Theoretical and experimental studies have converged on small E_a values (0.1-0.7 eV) for halogen vacancy formation and migration in halide perovskites [57,58,62,64,65]. By contrast, oxide perovskites exhibit higher E_a values (>0.5 eV) [65,66] attributed to increased lattice energy due to

Box 1. Halogen point defects and mixed ionic-electronic conductivity in halide perovskites

Several halide perovskites are mixed ionic–electronic conductors. These perovskite semiconductors exhibit bandgap energies greater than 1 eV (see Figure 2A in main text); thus, the dark electrical conductivity derives from intrinsic carrier concentrations (Figure IA, left) or carrier concentrations modified through doping. The addition of donors generates an excess electron concentration (*n*-type doping; Figure IA, middle), whereas acceptors generate an excess hole concentration (*p*-type doping; Figure IA, right). Bulk ionic conductivity in the halide perovskites is attributed to mobile point defects, particularly halogen vacancies, in analogy to the well-established relationship between oxygen vacancies and oxide mobility in oxide perovskites. Halide (X^-) loss results in a positively charged vacancy or point defect, which must be compensated by another charged defect or charge carrier (holes or electrons). Among the possible halogen vacancy–based defect reactions, halogen off-gassing (positively charged halogen vacancies compensated by electrons; Figure IB, top left), Schottky disorder (positively charged halogen vacancies compensated by cation vacancies; Figure IB, top right), and anti-Frenkel disorder (positively charged halogen vacancies compensated by negatively charged halogen interstitials; Figure IB, bottom) have been the focus of investigation in the defect chemistry of the halide perovskites. Bulk halide conductivity occurs due to the presence of halogen vacancies and has been proposed to follow a vacancy-assisted hopping mechanism (Figure IC). Ionic conductivity was established using solid-state electrochemistry techniques, particularly electrolysis of coulometric reaction cells based on $CsPbBr_3$ (Figure ID, top) [57], $CsPbCl_3$ (identical construction and measurement as $CsPbBr_3$; not shown) [57], and $(CH_3NH_3)PbI_3$ (Figure ID, bottom) [44]. Direct current is applied to the cell, and the three possible outcomes indicate the nature of ion conduction. For example, (i) if the perovskite $CsPbBr_3$ is an anion conductor, Br^- migration from the perovskite produces $PbBr_2$ at the Pb–perovskite interface (the bromide is replenished by the AgBr layer) and a gravimetric gain of Br occurs on the left-hand side of the cell; (ii) if the perovskite is a cation conductor, Cs^+ or Pb^{2+} migration from the perovskite produces CsBr or $PbBr_2$, respectively, at the perovskite–AgBr interface and a gravimetric gain of Cs or Pb occurs on the right-hand side of the cell; (iii) if the perovskite is not an ion conductor, no change is observed. Analysis of the $CsPbBr_3$ cell after electrolysis indicated a gravimetric gain of the left-hand side of the cell, indicating that bromide was the dominant mobile ion. Similarly, diffraction, spectroscopy, and microscopy evidenced a reaction at the Pb–perovskite interface ($Pb^{2+} + 2I^- \rightarrow PbI_2$) after electrolysis of the $(CH_3NH_3)PbI_3$ cell, demonstrating that iodide was the dominant mobile ion.

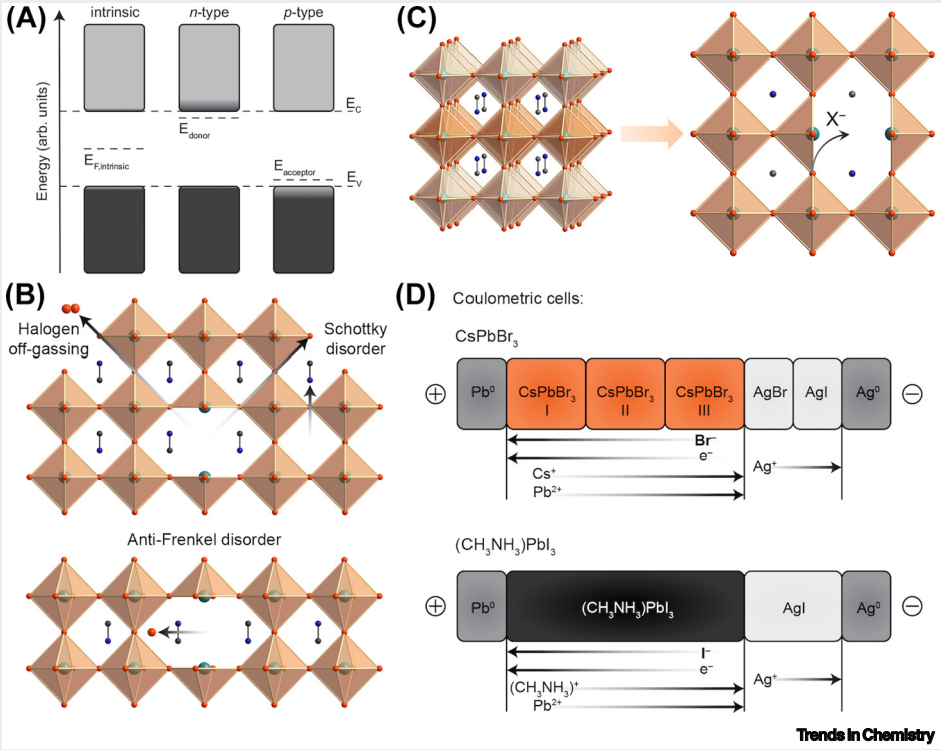

Figure I. Halogen point defects and mixed ionic-electronic conductivity in the halide perovskites. (A) Schematic block band diagram for a semiconductor (with conduction and valence band-edge energies of E_C and E_V, respectively) in three states: intrinsic (left, with a Fermi level at $E_{F,intrinsic}$), *n*-type (middle, with an electron donor level at E_{donor}), and *p*-type (right, with an electron acceptor level at $E_{acceptor}$). (B) Schematic of representative vacancy (top) and vacancy-interstitial (bottom) defect reactions in the perovskite structure; top: beginning with a positively charged vacancy (center), charge is balanced either with an electron (not shown) in the halogen off-gassing reaction producing $0.5X_2$ per halogen vacancy (left) or with a negatively charged cation vacancy (right, Schottky); bottom: the positively charged vacancy is charged balanced by the formation of a negatively charged interstitial (anti-Frenkel). (C) Schematic of vacancy-assisted halide migration in a slice of the 3D cubic perovskite structure, where X^- signifies the mobile halide. Turquoise, orange, blue, and gray spheres represent Pb, Br, N, and C atoms, respectively. Hydrogen atoms are omitted for clarity. (D) Coulometric cell configurations in solid-state electrochemistry and interfacial reactivity studies of $CsPbBr_3$ [57] and $(CH_3NH_3)PbI_3$ [44], including the expected direction of ionic drift for potential mobile ions; the $CsPbBr_3$ cell comprised three distinct pellets of $CsPbBr_3$ for separate gravimetric analysis.

higher-valent metals in the oxides [66]. Apart from $(CH_3NH_3)PbI_3$, facile formation and transport of halogen vacancies have been calculated or observed indirectly in a number of 3D inorganic perovskites including $CsMX_3$ ($M = Sn^{2+}$, Pb^{2+}; $X = Cl^-$, Br^-, I^-) and double perovskites ($Cs_2AgBiBr_6$ [67,68], Cs_2SnI_6 [69], and $Cs_2AgTlBr_6$ [70]).

Both **Schottky disorder** [66,71] and **anti-Frenkel disorder** [64,65] (see Figure IB in Box 1) have been proposed as the dominant defect reaction in first-principles modeling of $(CH_3NH_3)PbI_3$. The negative slope of the $\log(\sigma_{ion})$–$\log[p(I_2)]$ relationship (σ_{ion} = ionic conductivity) measured in cells with ion-blocking electrodes in the dark and under illumination, however, was decisively consistent with Schottky disorder [62,72]. Furthermore, conductivity measurements under $p(I_2)$ and illumination provide insights into the operational stability of perovskite-based devices, including halide segregation, space-charge formation, and accelerated degradation [12,72]. While changes in electronic

conductivity are expected upon illumination, changes in ionic conductivity are more difficult to predict. A two-order-of-magnitude increase in the ionic conductivity of $(CH_3NH_3)PbI_3$ upon illumination at only 15 mW cm^{-2} intensity has been observed [72]. The authors proposed that, upon illumination, an iodine interstitial/vacancy defect mechanism explains the concomitant increase in ionic and electronic conductivity, while the increased chemical potential of I^- drives accelerated degradation. A subsequent observation of reduced ionic conductivity enhancements under illumination in $(CH_3NH_3)PbBr_3$ and $CsPbBr_3$ was attributed to the lower polarizability of the bromide site (relative to the iodide) [73]. We expect that continued studies on the ionic conductivity of halide perovskites, as well as the separation of bulk, surface, and grain boundary transport processes, will significantly advance the field.

Even still, defect passivation approaches involving halide coordination or halogen vacancy filling have proven effective toward stabilizing and optimizing perovskite solar cells. Non-covalent halogen bonding between iodopentafluorobenzene (halogen bond donor) and undercoordinated iodides (halogen bond acceptor) at the surface of a $(CH_3NH_3)PbI_3$ film reduced hole trapping and charge accumulation at the interface with the hole transport layer [74]. Perovskite thin-film devices prepared in the presence of excess halide salt, particularly KI, exhibit reduced non-radiative recombination losses and halide migration instabilities [75]. The K^+ appears to reside primarily at the grain boundaries (surfaces) and the improved performance and stability are attributed to halogen vacancy filling.

Halide substitution and halogen off-gassing

Varying the identity and ratio of halides in the precursors often allows for the crystallization of perovskites with targeted halide compositions. However, the precursor halide ratio is not necessarily retained in the product, and we stress that elemental analysis on the bulk product is the best indicator of overall halide composition. Several intriguing postsynthetic halide-exchange strategies have also been developed (Figure 3A). Solid–liquid conversion reactions have proven efficient for halide exchange in polycrystalline perovskites. Exposure of the perovskite to an excess halide precursor solution, such as a dissolved lead-halide or ammonium-halide salt, affords complete or partial halide exchange [76–78]. Trimethylsilyl-halides [(TMS)X] also react with perovskite nanoparticles to exchange the halide, driven by the thermodynamic stability of the Si–X bond (bond strength: Si–Cl > Si–Br > Si–I) [79]. Thus, chloride or bromide perovskites can be converted to iodide perovskites using (TMS)I and chloride perovskites can be converted to bromide perovskites using (TMS)Br [79].

Gas–solid reactions can also exchange halides in perovskites. Exposing the perovskite to HX gas enables full or partial halide exchange [80]. Reactions with halogen gas exploit the reduction

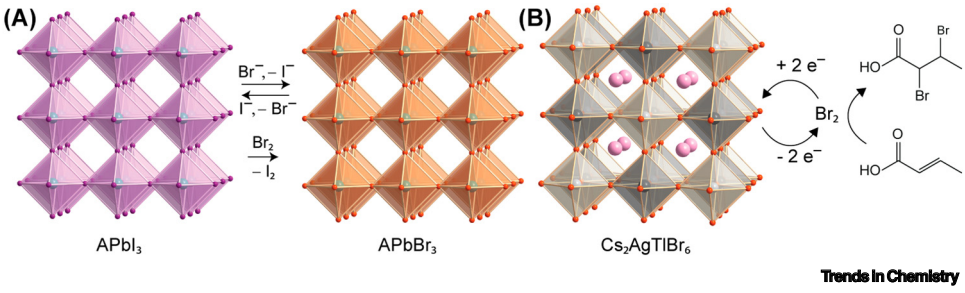

Figure 3. Halide substitution and halogen off-gassing in halide perovskites. (A) Schematic reaction for the halide exchange reaction in $APbX_3$ (X = I^-, Br^-) involving Br_2 gas or Br^-/I^- precursors. Adapted, with permission, from [81]. (B) Schematic showing reversible Br_2 off-gassing from $Cs_2AgTlBr_6$ and subsequent halogenation of crotonic acid. Octahedra comprising PbI_6, $PbBr_6$, $AgBr_6$, and $TlBr_6$ are shaded in purple, orange, white, and gray, respectively. Cs atoms are shown as pink spheres and the A-site cations in the lead perovskites are omitted for generality.

potentials of the halogen gas/halide couples (E^o Cl_2/Cl^- = 1.36 V, E^o Br_2/Br^- = 1.07 V; E^o I_2/I^- = 0.54 V) to drive the reaction between the halide in the perovskite and halogen gas (e.g., 2 I^- + Br_2 → I_2 + 2 Br^-, ΔE^o = 0.53 V; where the positive potential difference indicates reaction spontaneity) [81]. Thus, iodide perovskites can be converted to bromide or chloride perovskites using Br_2 or Cl_2 gas, respectively, and bromide perovskites can be converted to chloride perovskites using Cl_2 gas. Interestingly, the morphology of the parent film is preserved in the product despite the large atomic rearrangement resulting from this reaction [81].

Halogen redox chemistry can also influence the electronic conductivity, carrier concentration, and fermi level of halide perovskites [12,70,82]. The double perovskite $Cs_2AgTlBr_6$ displayed an increase in electronic conductivity upon spontaneous Br_2 off-gassing (Figure 3B), where the Br_2 was identified through the bromination of crotonic acid [70]. The increasing conductivity of the $Cs_2AgTlBr_6$ crystal upon Br_2 loss is consistent with *n*-type self-doping, or the defect reaction analogous to oxygen exchange

$$2Br_{Br}^{X} \rightleftharpoons 2V_{Br}^{\bullet} + 2e^{'} + Br_{2(g)} \quad [2]$$

where two bromine atoms leave the perovskite as Br_2, generating two monocationic bromine vacancies ($V_{Br}^{\bullet}$) and two electrons. Notably, this process is reversible, and the conductivity decreases upon exposing the perovskite to Br_2 gas. Similarly, I_2 exposure can modify the conductivity and fermi level of *p*-type $(CH_3NH_3)PbI_3$ [82]. Overall, halogen off-gassing in halide perovskites resembles doping of oxide perovskites via the oxygen exchange equilibrium [21], but at significantly lower temperatures.

Halide segregation under illumination

Bandgap tunability through halide mixing was initially considered a major advantage of perovskite photovoltaic absorbers. However, the higher-bandgap lead–bromide–iodide perovskites did not produce higher voltages than the pure-iodide perovskite absorbers [83]. McGehee, Karunadasa, *et al.* [42] showed that illumination causes transient changes in $(CH_3NH_3)Pb(Br_xI_{1-x})_3$ ($0.2 < x < 1$), evident in PL, transient absorbance spectra, and powder X-ray diffraction . These data were explained as a photo-induced phase segregation of the mixed-halide perovskite into I^-- and Br^--rich domains (Figure 4A). Here, the smaller-gap iodide-rich domains acted as traps that reduced the open-circuit potential and red-shifted the PL (Figure 4B). Surprisingly, the material restored its initial, homogeneously mixed composition after a few minutes in the dark. Further, bright nanodomains were identified after several seconds of illumination using cathodoluminescence, attributed to iodide-rich regions, starting at the grain boundaries (Figure 4C) [83]. While photo-induced halide segregation is now a well-accepted phenomenon, its origin and mechanism are still under investigation [13,14]. Models that explain halide segregation under illumination attribute the phenomenon to the metastability of mixed-halide perovskites [85], to polaron formation (photogenerated charge carriers and their accompanying lattice distortions) [84], or to photogenerated carrier gradients or electric fields at defects or interfaces [86–88].

Because of the importance of achieving a 1.7–1.8-eV bandgap perovskite as the top absorber in a tandem solar cell with Si, efforts have been devoted to eliminating photo-induced phase segregation in bromide-rich bromide–iodide perovskites. Increasing grain size and film crystallinity reduced this effect, further suggesting that halide mobility is highest at grain boundaries [13]. Introducing multiple A-site cations [$CH_3NH_3^+$, $CH(NH_2)_2^+$, Cs^+, and/or Rb^+] in mixed-halide perovskites can also reduce photo-induced halide segregation [34,89–93]. PL spectra of $(CH_3NH_3)Pb(Br_xI_{1-x})_3$ obtained at high pressures suggest that halide segregation is reduced with compression in the ambient-pressure α phase (0–0.9 GPa), and may be entirely suppressed in the high-

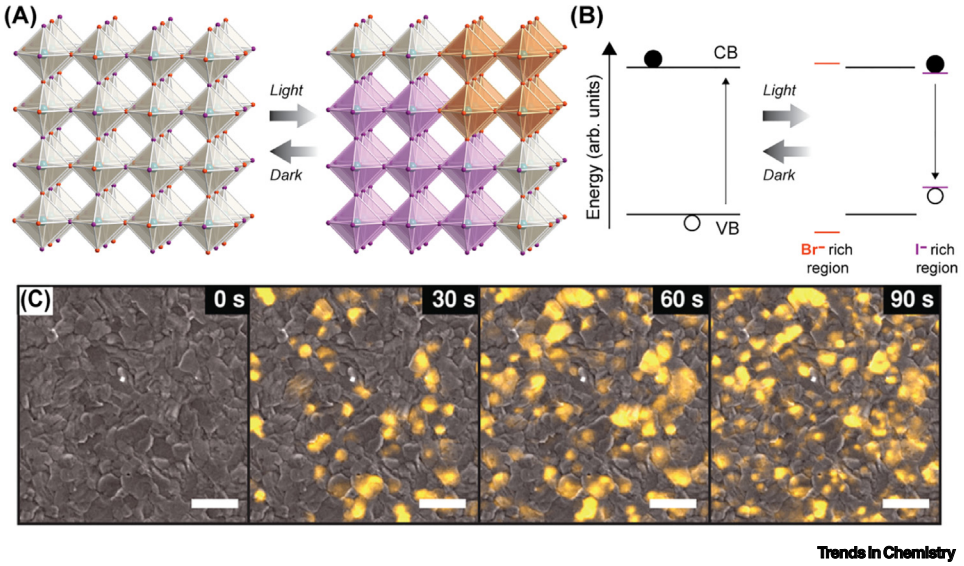

Figure 4. Photo-induced phase segregation in halide perovskites. (A) Schematic depiction of the reversible halide segregation under illumination that transforms a mixed-halide perovskite into Br^-- and I^--rich domains, shaded in orange and purple, respectively. A-site cations are omitted for clarity. Adapted, with permission, from [114]. (B) Schematic of the proposed band diagrams of the mixed-halide perovskites in the dark and under illumination. The band diagrams of the Br^-- and I^--rich regions are displayed in orange and purple, respectively, showing how I^--rich domains act as traps for photogenerated holes and electrons. Adapted, with permission, from [42]. (C) Cathodoluminescence images of polycrystalline $(CH_3NH_3)Pb(Br_{0.9}I_{0.1})_3$ after sequential light exposure in 30-s increments. The scale bar is 2 μm. The yellow regions are attributed to be iodide rich. Adapted, with permission, from [84].

pressure β phase. Thus, a stiffer lattice may kinetically suppress halide migration, or pressure may change the thermodynamics of halogen defect formation [94]. Indeed, the effects of mixed A-site cations on halide segregation may be a consequence of chemical pressure [12]. Recently, McGehee, Xu, and colleagues [93] explored triple-halide perovskites as stable absorbers. Single-phase perovskites with up to 15% Cl^- at the X-site were prepared by mixing $[CH(NH_2)_2]_{0.75}Cs_{0.25}Pb(Br_{0.2}I_{0.8})_3$ with $(CH_3NH_3)PbCl_3$ [93]. The resulting perovskite showed a bandgap (1.67 eV) close to the ideal value for a tandem device, while containing less bromide than bromide–iodide perovskites with similar bandgaps that show phase segregation. Thus, the triple-halide perovskite was resistant to phase segregation under 100-sun illumination [42,93].

Halogen capture and separation

Despite their close-packed structures, layered perovskites can intercalate various molecules through an 'accordion-like' expansion along the stacking direction of the inorganic sheets. Early work evidenced a reversible expansion when $(C_{10}H_{21}NH_3)_2CdCl_4$ was exposed to 1,2-dichlorobenzene or 1-chloronaphthalene [95]. Similarly, I_2 gas can intercalate into the 2D perovskite $(I\text{-}CH_2C_5H_{10}NH_3)_2PbI_4$ with a 33% lattice expansion along one axis (Figure 5A,B) [96]. Here, the polarizable I_2 molecules increase the dielectric constant of the organic layer, greatly reducing the binding energy of excitons in the inorganic sheets. The intercalated I_2 in $(I\text{-}CH_2C_5H_{10}NH_3)_2PbI_4{\cdot}2I_2$ is stabilized by halogen–halogen interactions between the terminal inorganic iodides and the organoiodides, producing a structure reminiscent of the triiodide ligand (I_3^-) in a 2D halide-pseudohalide perovskite $[NH_3(CH_2)_7NH_3]_2Au_2I_6(I_3)_2$ [97].

Halogen gas can also react with the molecules in the organic layers. Upon exposure to I_2 gas, the alkyne-perovskite $[HC{\equiv}C(CH_2)_2NH_3]_2PbBr_4$ generates the alkene-perovskite

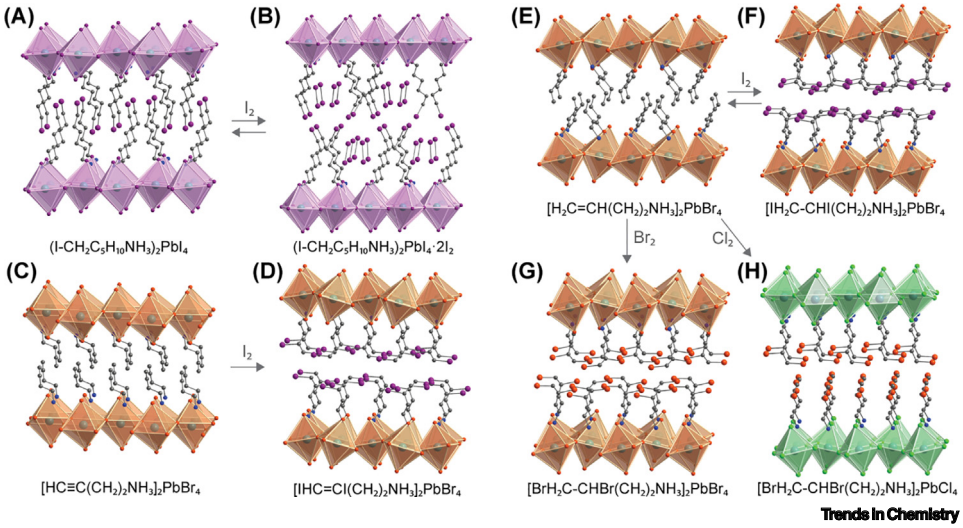

Figure 5. Halogen gas capture and separation in 2D halide perovskites. (A, B) I_2 gas intercalation in a 2D halide perovskite containing iodoalkane cations. (C–H) I_2, Br_2, or Cl_2 gas chemisorption in 2D halide perovskites containing organic cations with alkyne and alkene functionalities. Structures were determined by (A, C, D, E, G, H) single-crystal X-ray diffraction, (B) geometry optimization, or (F, the figure is a model) powder X-ray diffraction [81,96,98]. Octahedra comprising PbI_6, $PbBr_6$, and $PbCl_6$ are shaded in purple, orange, and green, respectively. Purple, orange, blue, and gray spheres represent I, Br, N, and C atoms, respectively; H atoms are omitted for clarity.

$[IHC{=}CI(CH_2)_2NH_3]_2PbBr_4$ (Figure 5C,D) [98]. This I_2 chemisorption made $[HC{\equiv}C(CH_2)_2NH_3]_2PbBr_4$ a promising candidate for radioactive $^{129}I_2$ gas capture from nuclear power plants. The perovskite showed an excellent volumetric capacity for I_2 gas (1.48 g cm^{-3}) and maintained 90% capacity under simulated operating conditions with moisture and NO_x gases.

Similarly, Br_2 and I_2 gas can convert the alkene-perovskite $[H_2C{=}CH(CH_2)_2NH_3]_2PbBr_4$ to the corresponding dihaloalkane-perovskites (Figure 5E–G) [81,98]. Akin to the solution-state stability of dihaloalkanes, the dibromoalkane-perovskite was stable (Figure 5G), whereas the diiodoalkane-perovskite spontaneously lost I_2 (Figure 5F). Here, the length of the alkyl chain in the diiodoalkane-perovskite could modulate the I_2 off-gassing rate through crystal packing effects [98]. Although halide separation through selective precipitation in solution is straightforward, gas-phase halogen separation is difficult. Irreversible Br_2 capture and reversible I_2 capture by $[H_2C{=}CH(CH_2)_2NH_3]_2PbBr_4$ can be used to scrub Br_2 and IBr from I_2/Br_2 mixtures, purifying I_2 gas streams.

Halide exchange through X_2/X^- redox chemistry can also yield unusual reactions in 2D perovskites. For example, upon Cl_2 exposure, the alkene-perovskite $[H_2C{=}CH(CH_2)_2NH_3]_2PbBr_4$ does not produce the dichloroalkane-perovskite. Instead, Cl_2 gas oxidizes Br^- in the inorganic sheets to Br_2, which then brominates the alkenes to afford $[BrH_2C\text{-}CHBr(CH_2)_2NH_3]_2PbCl_4$ (Figure 5H) [81]. Postsynthetic reactions can also afford 2D perovskites that cannot be formed in solution. For example, organoiodides cannot be incorporated into lead–bromide perovskites because Br^- attacks organoiodides in solution to form organobromides. However, stoichiometric Br_2 gas converts the 2D perovskite $(I\text{-}CH_2C_5H_{10}NH_3)_2PbI_4$ to $(I\text{-}CH_2C_5H_{10}NH_3)_2PbBr_4$, presumably due to the faster exchange kinetics of halogen substitution in the inorganic framework compared with halogen substitution at the organoiodides [96].

Halogen gas can also oxidize polymerized organic layers in 2D perovskites, increasing their conductivity. For example, a recent study reported a 1000-fold increase in conductivity in a

perovskite upon exposure to I_2 or O_2, attributed to hole doping of a conjugated polymer formed with deca-3,5-diyn-1-ammonium cations in the organic layer [99].

Pseudohalide perovskites

Pseudohalide perovskites maintain the perovskite structure with the X-site occupied by pseudohalides such as azides (N_3^-) [100], cyanides (CN^-) [101,102], dicyanamides [$N(CN)_2^-$] [103], formates ($HCOO^-$) [104], thiocyanates (SCN^-)[105,106], triiodides (I_3^-) [97], or borohydrides (BH_4^-) [107]. The elongated anions allow for larger A-site cations such as tetramethylammonium [$(CH_3)_4N^+$] in [$(CH_3)_4N$]$Mn(N_3)_3$ (Figure 6A) [100]. Similarly, formate and dicyanamide perovskites can incorporate cyclotrimethyleneamine [104] and benzyltributylammonium [103] as A-site cations, respectively.

The Prussian Blue analogs are a well-known family of coordination polymers with the generic formula $B[B'(CN)_6]$ [102]. The structure, named after $Fe^{III}[Fe^{II}(CN)_6]_{3/4}\cdot xH_2O$ (Prussian Blue), is analogous to that of 3D double perovskites, with vacancies in the A-sites and in one-fourth of the B′ sites (Figure 6B) [24,102]. Dimensional reduction of the Prussian Blue analogs produces the Hofmann clathrates, typified by $Ni(NH_3)(CN)_2\cdot C_6H_6$ (Figure 6C) [108]. This 2D structure, analogous to 2D halide perovskites, consists of layers of octahedrally coordinated metals with bridging cyanides and terminal amines, separated by benzene molecules [109,110].

Although halide and pseudohalide perovskites have evolved separately, materials with mixed ligands are beginning to be explored. The 2D double perovskite $[NH_3(CH_2)_7NH_3]_2Au_2I_6(I_3)_2$ [97] features both I^- and I_3^- ligands and I_2 intercalation into the iodide perovskite $(I\text{-}CH_2C_5H_{10}NH_3)_2PbI_4$ can postsynthetically yield terminal I_3^- ligands [96]. In the 2D perovskite $(CH_3NH_3)_2PbI_2(SCN)_2$ (Figure 1D), SCN^- ligands occupy the terminal X-site [105,106]. This Pb–I–SCN perovskite shows a decreased bandgap compared with analogous Pb–I perovskites [105,111], which has been partially attributed to decreased octahedral tilting [112]. Here, NH_3^+ groups only interact with SCN^- ligands, resulting in flat inorganic sheets. By contrast, typical 2D halide perovskites often display H bonding between the NH_3^+ groups and the bridging halides, inducing octahedral tilting. This mixed-ligand perovskite also displays an unusually low exciton binding energy, which may arise from an increased polarizability in the inorganic sheets due to the covalency in the Pb–S bond allowing for some delocalization of the π electrons in the thiocyanate group [105]. In addition, 2D infrared spectroscopy reveals ps-scale dynamics that occur in the inorganic

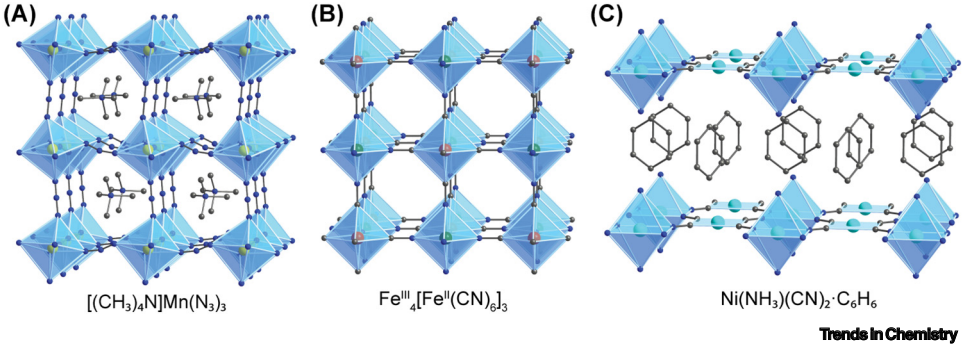

Figure 6. Crystal structures of halide-perovskite analogs containing pseudohalides. (A) A 3D pseudohalide perovskite, $[(CH_3)_4N]Mn(N_3)_3$. (B) Prussian blue, which can be considered a double perovskite with vacancies in the A sites and 25% of the B′ sites, $Fe^{III}_4[Fe^{II}(CN)_6]_3$. (C) A Hofmann clathrate, $Ni(NH_3)(CN)_2\cdot C_6H_6$, with analogies to 2D perovskites. Transition metal-N/C octahedra are shaded in blue. Disordered atoms and hydrogen atoms are omitted for clarity. Key: light green, Mn; dark green, Fe^{III}; orange, Fe^{II}; cyan, Ni; blue, N; gray, C.

framework within the vibrational lifetime of the C≡N stretch, indicating a highly fluxional structure [113]. Indeed this perovskite exhibits an uncommonly low bulk modulus (K_0 = 7.6 GPa) characteristic of a very soft structure [105]. Altogether, the Pb–I–SCN perovskite exemplifies how pseudohalide incorporation can substantially change the properties of a halide perovskite.

Concluding remarks

Oxide perovskites, often synthesized above 1000°C, exhibit O_2 loss and oxide anion conductivity at similarly high temperatures. It is thus not surprising that halide perovskites, which typically assemble at ambient temperature and pressure, lose halogen gas and conduct halides closer to room temperature. Furthermore, halide perovskites have softer lattices than the oxides, with bulk moduli that are lower by an order of magnitude. Thus, lattice dynamics [113] and compression effects [114] should be more pronounced in the halides, as seen in recent experiments. As the parallels between halide perovskites and their oxide analogs become clearer, we anticipate that researchers can better target the halogen chemistry of halide perovskites to improve their performance and stability in technological applications (see Outstanding questions). Further, layered hybrid perovskites provide a platform for chemistry not yet available in the oxides. Halogenation reactions enable halogen physisorption and chemisorption, halide exchange and halide transfer between organic and inorganic layers, and the synthesis of new perovskite compositions, including those that cannot be formed in solution. These transformations exemplify the richness of the halogen chemistry of 2D halide perovskites.

Outstanding questions

Can we draw further parallels between the well-known oxygen chemistry of oxide perovskites and the halogen chemistry of halide perovskites to improve our understanding of how to tune the halide site to access desired properties?

How can we apply our understanding of halide-based defects to synthesize new materials that are resistant to defects (e.g., materials that resist halogen off-gassing or HX loss) as well as materials that promote the formation of defects (e.g., materials that can be controllably doped through halogen loss or non-stoichiometry)?

Can pseudohalide perovskites and mixed-halide-pseudohalide perovskites show suitable bandgaps and band dispersion for optoelectronic applications?

Are complex postsynthetic reactions between perovskites and small molecules, where crystal packing affords products that cannot be isolated in solution, achievable by exploiting the chemistry of the halide site?

Acknowledgments

This work was supported by the U.S. Department of Energy, Office of Basic Energy Sciences, Division of Materials Sciences and Engineering, under Contract DE-AC02-76SF00515 (R.M.); Exxon Mobil through its membership in the Stanford Strategic Energy Alliance (J.A.V); the National Science Foundation, Division of Materials Research, under contract DMR-1904443 (E.J.C.). R.M. thanks Fundación Ramón Areces for a postdoctoral fellowship. J.A.V. acknowledges fellowship support from the Stanford University Office of the Vice Provost of Graduate Education and the National Science Foundation Graduate Research Fellowship Program under Grant No. DGE-1656518.

Declaration of interests

The authors have no competing financial interests to declare.

References

1. Berzelius, J.J. (1834) Untersuchung über die eigenschaften des tellurs. *Ann. Phys.* 108, 577–627
2. Cross, W. and Hillebrand, W.F. (1885) Contributions to the mineralogy of the rocky mountains. In *Bulletin of the United States Geological Survey No. 20*, pp. 57, Government Printing Office
3. Wells, H.L. (1893) Über die cäsium- und kalium-bleihalogenide. *Z. Anorg. Allg. Chem.* 3, 195–210
4. Elliott, N. and Pauling, L. (1938) The crystal structure of cesium aurous auric chloride, $Cs_2AuAuCl_6$, and cesium argentous auric chloride, $Cs_2AgAuCl_6$. *J. Am. Chem. Soc.* 60, 1846–1851
5. Kojima, A. *et al.* (2009) Organometal halide perovskites as visible-light sensitizers for photovoltaic cells. *J. Am. Chem. Soc.* 131, 6050–6051
6. Kim, H.-S. *et al.* (2012) Lead iodide perovskite sensitized all-solid-state submicron thin film mesoscopic solar cell with efficiency exceeding 9%. *Sci. Rep.* 2, 591
7. Lee, M.M. *et al.* (2012) Efficient hybrid solar cells based on meso-superstructured organometal halide perovskites. *Science* 338, 643
8. Protesescu, L. *et al.* (2015) Nanocrystals of cesium lead halide perovskites ($CsPbX_3$, X = Cl, Br, and I): novel optoelectronic materials showing bright emission with wide color gamut. *Nano Lett.* 15, 3692–3696
9. Smith, M.D. *et al.* (2019) Tuning the luminescence of layered halide perovskites. *Chem. Rev.* 119, 3104–3139
10. Chondroudis, K. and Mitzi, D.B. (1999) Electroluminescence from an organic–inorganic perovskite incorporating a quaterthiophene dye within lead halide perovskite layers. *Chem. Mater.* 11, 3028–3030
11. Lin, K. *et al.* (2018) Perovskite light-emitting diodes with external quantum efficiency exceeding 20 per cent. *Nature* 562, 245–248
12. Chen, Q. *et al.* (2018) All-inorganic perovskite nanocrystal scintillators. *Nature* 561, 88–93
13. Senocrate, A. and Maier, J. (2019) Solid-state ionics of hybrid halide perovskites. *J. Am. Chem. Soc.* 141, 8382–8396
14. Slotcavage, D.J. *et al.* (2016) Light-induced phase segregation in halide-perovskite absorbers. *ACS Energy Lett.* 1, 1199–1205
15. Brennan, M.C. *et al.* (2020) Photoinduced anion segregation in mixed halide perovskites. *Trends Chem.* 2, 282–301
16. Li, W. *et al.* (2017) Chemically diverse and multifunctional hybrid organic–inorganic perovskites. *Nat. Rev. Mater.* 2, 16099
17. Smith, I.C. *et al.* (2017) Between the sheets: postsynthetic transformations in hybrid perovskites. *Chem. Mater.* 29, 1868–1884
18. Bhalla, A.S. *et al.* (2000) The perovskite structure—a review of its role in ceramic science and technology. *Mater. Res. Innov.* 4, 3–26
19. Bednorz, J.G. and Müller, K.A. (1986) Possible high Tc superconductivity in the Ba–La–Cu–O system. *Z. Phys. B* 64, 189–193

20. Cava, R.J. (1993) Synthesis and crystal chemistry of high-Tc oxide superconductor. In *Processing and Properties of High-TC Superconductors* (Jin, S., ed.), pp. 492, World Scientific
21. Rao, C.N.R. (1990) Perovskite oxides and high-temperature superconductivity. *Ferroelectrics* 102, 297–308
22. Maier, J., ed (2004) *Physical Chemistry of Ionic Materials: Ions and Electrons in Solids*, John Wiley & Sons
23. Kharton, V.V. *et al.* (2004) Transport properties of solid oxide electrolyte ceramics: a brief review. *Solid State Ion.* 174, 135–149
24. Wolf, N.R. *et al.* (2021) Doubling the stakes: the promise of halide double perovskites. *Angew. Chem. Int. Ed.* 60, 16264–16278
25. Saparov, B. and Mitzi, D.B. (2016) Organic–inorganic perovskites: structural versatility for functional materials design. *Chem. Rev.* 116, 4558–4596
26. Smith, M.D. *et al.* (2018) The diversity of layered halide perovskites. *Annu. Rev. Mater. Res.* 48, 111–136
27. Natta, G. and Passerini, L. (1928) Isomorphism, polymorphism and morphotropy, I. Compounds of the ABX_3 type. *Gazz. Chim. Ital.* 58, 472–484
28. Horowitz, A. *et al.* (1982) Structure types and phase transformations in $KMnCl_3$ and $TlMnCl_3$. *J. Solid State Chem.* 43, 107–125
29. Travis, W. *et al.* (2016) On the application of the tolerance factor to inorganic and hybrid halide perovskites: a revised system. *Chem. Sci.* 7, 4548–4556
30. Goldschmidt, V.M. (1926) Die gesetze der krystallochemie. *Naturwissenschaften* 14, 477–485
31. Filip, M.R. and Giustino, F. (2018) The geometric blueprint of perovskites. *Proc. Natl. Acad. Sci. U. S. A.* 115, 5397–5402
32. Bartel, C.J. *et al.* (2019) New tolerance factor to predict the stability of perovskite oxides and halides. *Sci. Adv.* 5, aav0693
33. Steele, J.A. *et al.* (2021) Trojans that flip the black phase: impurity-driven stabilization and spontaneous strain suppression in γ-$CsPbI_3$ perovskite. *J. Am. Chem. Soc.* 143, 10500–10508
34. Beal, R.E. *et al.* (2020) Structural origins of light-induced phase segregation in organic-inorganic halide perovskite photovoltaic materials. *Matter* 2, 207–219
35. Connor, B.A. *et al.* (2020) Dimensional reduction of the small-bandgap double perovskite $Cs_2AgTlBr_6$. *Chem. Sci.* 11, 7708–7715
36. Lemmerer, A. and Billing, D.G. (2010) Effect of heteroatoms in the inorganic–organic layered perovskite-type hybrids $[(ZC_nH_{2n}NH_3)_2PbI_4]$, n = 2, 3, 4, 5, 6; Z = OH, Br and I; and $[(H_3NC_2H_4S_2C_2H_4NH_3)PbI_4]$. *CrystEngComm* 12, 1290–1301
37. Suzuki, Y. and Kubo, H. (1983) Distribution of Cl^- and Br^- ions in mixed crystals $(CH_3NH_3)_2Cu(Cl_{1-x}Br_x)_4$. *J. Phys. Soc. Jpn.* 52, 1420–1426
38. Sourisseau, S. *et al.* (2007) Hybrid perovskite resulting from the solid-state reaction between the organic cations and perovskite layers of α1-$(Br\text{-}(CH_2)_2\text{-}NH_3)_2PbI_4$. *Inorg. Chem.* 46, 6148–6154
39. Umebayashi, T. *et al.* (2003) Electronic structures of lead iodide based low-dimensional crystals. *Phys. Rev. B* 67, 155405
40. Goesten, M.G. and Hoffmann, R. (2018) Mirrors of bonding in metal halide perovskites. *J. Am. Chem. Soc.* 140, 12996–13010
41. Kepenekian, M. and Even, J. (2017) Rashba and Dresselhaus couplings in halide perovskites: accomplishments and opportunities for spintronics and spin–orbitronics. *J. Phys. Chem. Lett.* 8, 3362–3370
42. Hoke, E.T. *et al.* (2015) Reversible photo-induced trap formation in mixed-halide hybrid perovskites for photovoltaics. *Chem. Sci.* 6, 613–617
43. Slavney, A.H. *et al.* (2019) A pencil-and-paper method for elucidating halide double perovskite band structures. *Chem. Sci.* 10, 11041–11053
44. Yang, T.-Y. *et al.* (2015) The significance of ion conduction in a hybrid organic–inorganic lead-iodide-based perovskite photosensitizer. *Angew. Chem. Int. Ed.* 54, 7905–7910
45. Lanty, G. *et al.* (2014) Room-temperature optical tunability and inhomogeneous broadening in 2D-layered organic–inorganic perovskite pseudobinary alloys. *J. Phys. Chem. Lett.* 5, 3958–3963
46. Kitazawa, N. (1997) Excitons in two-dimensional layered perovskite compounds: $(C_6H_5C_2H_4NH_3)_2Pb(Br,I)_4$ and $(C_6H_5C_2H_4NH_3)_2Pb(Cl,Br)_4$. *Mater. Sci. Eng. B* 49, 233–238
47. Smith, M.D. and Karunadasa, H.I. (2018) White-light emission from layered halide perovskites. *Acc. Chem. Res.* 51, 619–627
48. Dohner, E.R. *et al.* (2014) Self-assembly of broadband white-light emitters. *J. Am. Chem. Soc.* 136, 1718–1721
49. Dohner, E.R. *et al.* (2014) Intrinsic white-light emission from layered hybrid perovskites. *J. Am. Chem. Soc.* 136, 13154–13157
50. Snaith, H.J. *et al.* (2014) Anomalous hysteresis in perovskite solar cells. *J. Phys. Chem. Lett.* 5, 1511–1515
51. Meloni, S. *et al.* (2016) Ionic polarization-induced current–voltage hysteresis in $CH_3NH_3PbX_3$ perovskite solar cells. *Nat. Commun.* 7, 10334
52. Xiao, Z. *et al.* (2015) Giant switchable photovoltaic effect in organometal trihalide perovskite devices. *Nat. Mater.* 14, 193–198
53. Juarez-Perez, E.J. *et al.* (2014) Photoinduced giant dielectric constant in lead halide perovskite solar cells. *J. Phys. Chem. Lett.* 5, 2390–2394
54. Wilson, J.N. *et al.* (2019) Dielectric and ferroic properties of metal halide perovskites. *APL Mater.* 7, 5079633
55. Bertoluzzi, L. *et al.* (2020) Mobile ion concentration measurement and open-access band diagram simulation platform for halide perovskite solar cells. *Joule* 4, 109–127
56. Lopez-Varo, P. *et al.* (2017) Effects of ion distributions on charge collection in perovskite solar cells. *ACS Energy Lett.* 2, 1450–1453
57. Mizusaki, J. *et al.* (1983) Ionic conduction of the perovskite-type halides. *Solid State Ion.* 11, 203–211
58. Yamada, K. *et al.* (1995) Chloride ion conductor $CH_3NH_3GeCl_3$ studied by Rietveld analysis of X-ray diffraction and ^{35}Cl NMR. *Solid State Ion.* 79, 152–157
59. Yamada, K. *et al.* (1998) Phase transition and electric conductivity of $ASnCl_3$ (A = Cs and CH_3NH_3). *Bull. Chem. Soc. Jpn.* 71, 127–134
60. Maeda, M. *et al.* (1997) Dielectric studies on $CH_3NH_3PbX_3$ (X = Cl and Br) single crystals. *J. Phys. Soc. Jpn.* 66, 1508–1511
61. Azpiroz, J.M. *et al.* (2015) Defect migration in methylammonium lead iodide and its role in perovskite solar cell operation. *Energy Environ. Sci.* 8, 2118–2127
62. Senocrate, A. *et al.* (2017) The nature of ion conduction in methylammonium lead iodide: a multimethod approach. *Angew. Chem. Int. Ed.* 56, 7755–7759
63. Senocrate, A. *et al.* (2018) Slow $CH_3NH_3^+$ diffusion in $CH_3NH_3PbI_3$ under light measured by solid-state NMR and tracer diffusion. *J. Phys. Chem. C* 122, 21803–21806
64. Barboni, D. and De Souza, R.A. (2018) The thermodynamics and kinetics of iodine vacancies in the hybrid perovskite methylammonium lead iodide. *Energy Environ. Sci.* 11, 3266–3274
65. De Souza, R.A. and Barboni, D. (2019) Iodide-ion conduction in methylammonium lead iodide perovskite: some extraordinary aspects. *Chem. Commun.* 55, 1108–1111
66. Walsh, A. *et al.* (2015) Self-regulation mechanism for charged point defects in hybrid halide perovskites. *Angew. Chem. Int. Ed.* 54, 1791–1794
67. Pan, W. *et al.* (2017) $Cs_2AgBiBr_6$ single-crystal X-ray detectors with a low detection limit. *Nat. Photonics* 11, 726–732
68. Slavney, A.H. *et al.* (2016) A bismuth-halide double perovskite with long carrier recombination lifetime for photovoltaic applications. *J. Am. Chem. Soc.* 138, 2138–2141
69. Xiao, Z. *et al.* (2015) Intrinsic defects in a photovoltaic perovskite variant Cs_2SnI_6. *Phys. Chem. Chem. Phys.* 17, 18900–18903
70. Slavney, A.H. *et al.* (2018) Small-band-gap halide double perovskites. *Angew. Chem. Int. Ed.* 57, 12765–12770
71. Eames, C. *et al.* (2015) Ionic transport in hybrid lead iodide perovskite solar cells. *Nat. Commun.* 6, 8497
72. Kim, G.Y. *et al.* (2018) Large tunable photoeffect on ion conduction in halide perovskites and implications for photodecomposition. *Nat. Mater.* 17, 445–449
73. Kim, G.Y. *et al.* (2021) Photo-effect on ion transport in mixed cation and halide perovskites and implications for photodemixing. *Angew. Chem. Int. Ed.* 60, 820–826
74. Abate, A. *et al.* (2014) Supramolecular halogen bond passivation of organic–inorganic halide perovskite solar cells. *Nano Lett.* 14, 3247–3254
75. Abdi-Jalebi, M. *et al.* (2018) Maximizing and stabilizing luminescence from halide perovskites with potassium passivation. *Nature* 555, 497–501

76. Pellet, N. *et al.* (2015) Transforming hybrid organic inorganic perovskites by rapid halide exchange. *Chem. Mater.* 27, 2181–2188
77. Nedelcu, G. *et al.* (2015) Fast anion-exchange in highly luminescent nanocrystals of cesium lead halide perovskites ($CsPbX_3$, X = Cl, Br, I). *Nano Lett.* 15, 5635–5640
78. Akkerman, Q.A. *et al.* (2015) Tuning the optical properties of cesium lead halide perovskite nanocrystals by anion exchange reactions. *J. Am. Chem. Soc.* 137, 10276–10281
79. Creutz, S.E. *et al.* (2018) Anion exchange in cesium lead halide perovskite nanocrystals and thin films using trimethylsilyl halide reagents. *Chem. Mater.* 30, 4887–4891
80. Chen, K. *et al.* (2016) Pseudomorphic transformation of organometal halide perovskite using the gaseous hydrogen halide reaction. *Chem. Mater.* 28, 5530–5537
81. Solis-Ibarra, D. *et al.* (2015) Post-synthetic halide conversion and selective halogen capture in hybrid perovskites. *Chem. Sci.* 6, 4054–4059
82. Zohar, A. *et al.* (2017) What is the mechanism of $MAPbI_3$ p-doping by I_2? Insights from optoelectronic properties. *ACS Energy Lett.* 2, 2408–2414
83. Noh, J.H. *et al.* (2013) Chemical management for colorful, efficient, and stable inorganic–organic hybrid nanostructured solar cells. *Nano Lett.* 13, 1764–1769
84. Bischak, C.G. *et al.* (2017) Origin of reversible photoinduced phase separation in hybrid perovskites. *Nano Lett.* 17, 1028–1033
85. Brivio, F. *et al.* (2016) Thermodynamic origin of photoinstability in the $CH_3NH_3Pb(I_{1-x}Br_x)_3$ hybrid halide perovskite alloy. *J. Phys. Chem. Lett.* 7, 1083–1087
86. Knight, A.J. *et al.* (2019) Electronic traps and phase segregation in lead mixed-halide perovskite. *ACS Energy Lett.* 4, 75–84
87. Barker, A.J. *et al.* (2017) Defect-assisted photoinduced halide segregation in mixed-halide perovskite thin films. *ACS Energy Lett.* 2, 1416–1424
88. Belisle, R.A. *et al.* (2018) Impact of surfaces on photoinduced halide segregation in mixed-halide perovskites. *ACS Energy Lett.* 3, 2694–2700
89. Hu, M. *et al.* (2016) Stabilized wide bandgap $MAPbBr_xI_{3-x}$ perovskite by enhanced grain size and improved crystallinity. *Adv. Sci.* 3, 201500301
90. Rehman, W. *et al.* (2017) Photovoltaic mixed-cation lead mixed-halide perovskites: links between crystallinity, photostability and electronic properties. *Energy Environ. Sci.* 10, 361–369
91. McMeekin, D.P. *et al.* (2016) A mixed-cation lead mixed-halide perovskite absorber for tandem solar cells. *Science* 351, 151–155
92. Correa-Baena, J.-P. *et al.* (2019) Homogenized halides and alkali cation segregation in alloyed organic-inorganic perovskites. *Science* 363, 627–631
93. Xu, J. *et al.* (2020) Triple-halide wide-band gap perovskites with suppressed phase segregation for efficient tandems. *Science* 367, 1097–1104
94. Jaffe, A. *et al.* (2016) High-pressure single-crystal structures of 3D lead-halide hybrid perovskites and pressure effects on their electronic and optical properties. *ACS Cent. Sci.* 2, 201–209
95. Dolzhenko, Y.I. *et al.* (1986) *In situ* X-ray observation on the intercalation of weak interaction molecules into perovskite-type layered crystals $(C_9H_{19}NH_3)_2PbI_4$ and $(C_{10}H_{21}NH_3)_2CdCl_4$. *Bull. Chem. Soc. Jpn.* 59, 563–567
96. Smith, M.D. *et al.* (2017) Decreasing the electronic confinement in layered perovskites through intercalation. *Chem. Sci.* 8, 1960–1968
97. Castro-Castro, L.M. and Guloy, A.M. (2003) Organic-based layered perovskites of mixed-valent gold(I)/gold(III) iodides. *Angew. Chem. Int. Ed.* 42, 2771–2774
98. Solis-Ibarra, D. and Karunadasa, H.I. (2014) Reversible and irreversible chemisorption in nonporous-crystalline hybrids. *Angew. Chem. Int. Ed.* 53, 1039–1042
99. Ortiz-Cervantes, C. *et al.* (2018) Thousand-fold conductivity increase in 2D perovskites by polydiacetylene incorporation and doping. *Angew. Chem. Int. Ed.* 57, 13882–13886
100. Mautner, F.A. *et al.* (1996) $[N(CH_3)_4][Mn(N_3)_3]$: a compound with a distorted perovskite structure through azido ligands. *Angew. Chem. Int. Ed.* 35, 78–80
101. Frisch, J.L. (1710) Miscellanea berolinensia ad incrementum scientiarum. In *Notitia Coerulei Berolinensis Nuper Inventi*, pp. 377, Societati Regiae Scientiarum
102. Buser, H.J. *et al.* (1977) The crystal structure of Prussian Blue: $Fe_4[Fe(CN)_6]_3{\cdot}xH_2O$. *Inorg. Chem.* 16, 2704–2710
103. Tong, M.-L. *et al.* (2003) Cation-templated construction of three-dimensional α-Po cubic-type $[M(dca)_3]^-$ networks. Syntheses, structures and magnetic properties of $A[M(dca)_3]$ (dca = dicyanamide; for A = benzyltributylammonium, M = Mn^{2+}, Co^{2+}; for A = benzyltriethylammonium, M = Mn^{2+}, Fe^{2+}). *New J. Chem.* 27, 779–782
104. Wang, Z. *et al.* (2004) Anionic NaCl-type frameworks of $[Mn^{II}(HCOO)_3^-]$, templated by alkylammonium, exhibit weak ferromagnetism. *Dalton Trans.* 2209–2216
105. Umeyama, D. *et al.* (2016) Red-to-black piezochromism in a compressible Pb-I-SCN layered perovskite. *Chem. Mater.* 28, 3241–3244
106. Daub, M. and Hillebrecht, H. (2015) Synthesis, single-crystal structure and characterization of $(CH_3NH_3)_2Pb(SCN)_2I_2$. *Angew. Chem. Int. Ed.* 54, 11016–11017
107. Schouwink, P. *et al.* (2014) Structure and properties of complex hydride perovskite materials. *Nat. Commun.* 5, 6706
108. Hofmann, K.A. and Küspert, F. (1897) Verbindungen von kohlenwasserstoffen mit metallsalzen. *Z. Anorg. Allg. Chem.* 15, 204–207
109. Rayner, J.H. and Powell, H.M. (1952) Structure of molecular compounds. Part X. Crystal structure of the compound of benzene with an ammonia–nickel cyanide complex. *J. Chem.* Soc, 319–328
110. Iwamoto, T. (1996) Past, present and future of the clathrate inclusion compounds built of cyanometallate hosts. *J. Incl. Phenom. Mol. Recognit. Chem.* 24, 61–132
111. Xiao, Z. *et al.* (2016) Photovoltaic properties of two-dimensional $(CH_3NH_3)_2Pb(SCN)_2I_2$ perovskite: a combined experimental and density functional theory study. *J. Phys. Chem. Lett.* 7, 1213–1218
112. Sourisseau, S. *et al.* (2007) Reduced band gap hybrid perovskites resulting from combined hydrogen and halogen bonding at the organic–inorganic interface. *Chem. Mater.* 19, 600–607
113. Nishida, J. *et al.* (2018) Dynamically disordered lattice in a layered Pb-I-SCN perovskite thin film probed by two-dimensional infrared spectroscopy. *J. Am. Chem. Soc.* 140, 9882–9890
114. Jaffe, A. *et al.* (2017) Halide perovskites under pressure: accessing new properties through lattice compression. *ACS Energy Lett.* 2, 1549–1555